IEEE Access
Multidisciplinary ⋮ Rapid Review ⋮ Open Access Journal

Received 4 June 2024, accepted 14 July 2024, date of publication 19 July 2024, date of current version 29 July 2024.

Digital Object Identifier 10.1109/ACCESS.2024.3431275

RESEARCH ARTICLE

Continuous Phase Modulation Proposal for Photonics-Wireless Sub-THz Transmissions

PAUL DESOMBRE[1,2], (Member, IEEE), HAÏFA FARÈS[2], (Member, IEEE), AND YVES LOUËT[2]
[1]IETR, UMR, CNRS, 6164, Université de Rennes, 35042 Rennes, France
[2]IETR, UMR, CNRS, 6164, CentraleSupélec-Rennes Campus, 35576 Cesson-Sévigné, France

Corresponding author: Paul Desombre (paul.desombre@centralesupelec.fr)

This work was supported by French Government granted to the Labex CominLabs Laboratory of Excellence and Managed by French National Research Agency Within the Framework of the "Investments of the Future" Program under Grant ANR-10-LABX-07-01.

ABSTRACT This paper presents a waveform proposal for photonic-wireless sub-THz transmissions. The concept of Continuous Phase Modulation (CPM) is first explained. Then, a mathematical model to simulate non-linear effects from photodiodes for the Amplitude-to-Amplitude (AM-AM) and a second model for the Amplitude-to-Phase (AM-PM) transfer functions is given. These models are then used to quantify non-linearities effects on linear waveforms (M-QAM) and non-linear waveforms (CPM). Afterwards, the communications range gained from using CPM over M-QAM from the simulated non-linear effects is calculated. To further appeal to the use of CPM, a study on energy efficiency is proposed. Finally, a proof of concept is given by experimentally comparing the CPM waveforms with a regular linear modulation, such as QPSK. An error-free data rate of 7.5 GBauds with Raised-Cosine, Gaussian Minimum Shift Keying (two CPM waveforms), and QPSK at a 107.5 GHz wireless 1-meter link is measured. To further estimate the robustness of the wireless link, a simulation of a communication with different transmit powers is done by adding white Gaussian noise to the acquired signals.

INDEX TERMS Continuous phase modulations, energy efficiency, photodiodes non-linearities, radio-over-fiber, sub-THz wireless communication, THz photonics.

I. INTRODUCTION

In the recent years, photonics-based sub-THz (100 GHz - 300 GHz) and THz (0.3 THz - 10 THz) communications have known many advances [1], [2], [3]. It has been accepted as a key enabling technology for future wireless standards as 6G and beyond era [4]. Chaccour et al. [5] describe the key defining features of sub-THz and THz wireless communications: quasi-opticality of the band, THz tailored wireless architectures, synergy with lower frequency bands, joint sensing, and communication systems, physical layer procedures, spectrum access techniques, and real-time network optimization.

Most of the work in wireless-photonics sub-THz communications is done using linear waveforms, such as M-QAM [3], [6], [7], [8], [9], [10], [11], or even On-Off Keying [12], [13], [14]. Very few work focus on exploring other waveforms [15], [16], [17], [18]. Fig. 1 present an overview of the current state-of-the-art in sub-THz communications. The squares stand for experimental photonics-based wireless sub-THz communications, while diamonds are for full electronics experiments. The color code is for carrier frequency.

As explained by the Ducournau et al. in [1], the research community has been focusing on the race for data rate. In contrast, this work focuses on energy efficiency and robustness to impairments, such as phase noise and non-linearities. Indeed, previous work showed that in case of communications impaired by phase noise, such as sub-THz wireless communications, Continuous Phase Modulation (CPM) could be a good alternative [19]. This work compared several waveforms against medium-to-high phase noise using five metrics: bit error rate, error vector magnitude, spectral efficiency, adjacent channel power ratio and peak-to-average power ratio. Authors from [20] previously investigated the use of CPM in optical fiber communications. Their main goal

The associate editor coordinating the review of this manuscript and approving it for publication was Chen Chen.

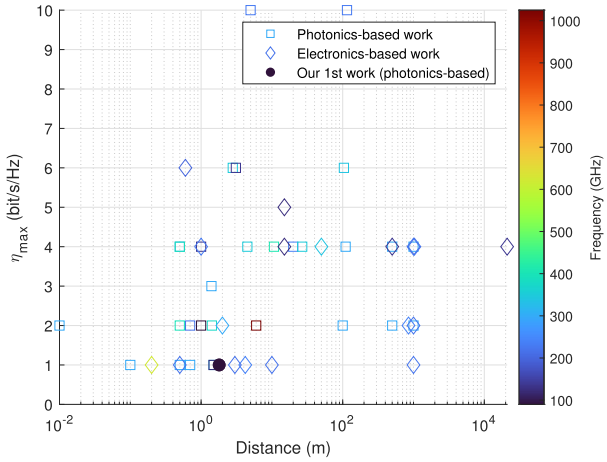

FIGURE 1. Sub-THz communications state-of-the-art: spectral efficiency (bits/s/Hz) vs Distance (m).

was to compare CPM with linear modulations, such as QPSK, in a 112 Gbit/s wired optical link.

This paper proposes an unexplored waveform design for the physical layer of sub-THz communications, relying on photonics frequency up-conversion techniques. A 7.5 GBauds photonics-based wireless transmission link over a 1 m range is used. The carrier frequency is 107.5 GHz, which is low compared to what the photonics research community has been using so far [3]. This low frequency is due to the cost and availability of higher-frequency equipment. A commercial photo-mixing antenna is used as a sub-THz transmitter. The originality of the proposed study comes from the experimental use of CPM modulations such as Raised-Cosine (RC) and Gaussian Minimum Shift Keying (GMSK). This paper is the continuation of previous work [21], where the use of GMSK in a low-bandwidth 90 GHz photonics-based transmission was explored. GMSK is a CPM used in the 2nd generation of mobile communications [22]. To the best of our knowledge, this journal is the first paper reporting the use of broadband CPM waveforms in an experimental sub-THz context.

The main contributions of this paper are as follows:

1) A novel mathematical model to accurately replicate non-linear effects induced by photodiodes in optical communication systems is introduced. Drawing upon an extensive literature review, this model is designed to aid researchers and engineers in optimizing optical communication chains.
2) This mathematical model is used to compare linear waveforms such as QPSK or 16-QAM with non-linear waveforms such as CPM (RC & GMSK). This study numerically proves the robustness of CPM against non-linear effects.
3) Using the non-linearities model presented earlier, and in a photonic-wireless sub-THz communications context, the wireless communication range is calculated. This shows that, for long range communications, CPM is an excellent candidate.
4) To further appeal on the use of CPM, an energy efficiency versus spectral efficiency model is presented and modified to integrate the power loss due to photodiodes. It is then used to compare long and short range communications in terms of energy efficiency and spectral efficiency. In a long-range communications scheme, where energy consumption is a key element, it is shown that M-ary CPM allows the use of the system optimally.
5) Experiments with a short-range wireless-photonic sub-THz link at 107.5 GHz are then presented. Link budget is given and analyzed. QPSK, GMSK and RC waveforms are compared in terms of Bit Error Rate performances and spectral occupation. The figure presenting the sub-THz state-of-the-Art is then updated with this work and the perspectives opened by the use of CPM waveforms.

The remainder of this paper is organized as follows: first, CPM pulse shaping techniques are mathematically described. Then, a photodiode non-linearities mathematical model is given in Amplitude-to-Amplitude (AM-AM) and Amplitude-to-Phase (AM-PM) transfer. This model is then used to compare CPM waveforms with M-QAM on several metrics. Next, a modified energy efficiency versus spectral efficiency model is used to compare short-range and long-range communications in the sub-THz bands in terms of energy efficiency. Afterwards, an experimental setup using CPM and QPSK is shown, and results are given. Then, future approach and practical use are discussed. Finally, conclusions are drawn.

II. CONTINUOUS PHASE MODULATION

Continuous Phase Modulation is a family of digital modulations with a constant envelope; the information is transmitted through the signal phase, and the phase variations are continuous. Such signal is mathematically expressed as [23]:

$$s(t) = \sqrt{\frac{E_s}{T_s}} \exp\left\{ j2\pi \sum_{i=-\infty}^{\infty} \alpha_i h \mathrm{q}(t - iT_s) \right\}, \qquad (1)$$

with E_s the symbol energy, T_s the symbol time, α_i the i-th M-ary transmitted symbol, $h \in \mathbb{Q}$ the modulation index and $\mathrm{q}(t)$ the phase response, represented as:

$$\mathrm{q}(t) = \begin{cases} 0 & t < 0, \\ \displaystyle\int_{-\infty}^{t} \mathrm{g}(\tau) d\tau & 0 \le t < LT_s, \\ 1/2 & t \ge LT_s, \end{cases} \qquad (2)$$

where $\mathrm{g}(t)$ is the frequency pulse, with a pulse length of $L \in \mathbb{N}^*$. When $L = 1$, the signal is said to be *full response*, while with $L > 1$, it is said as *partial response*. L is the memory depth of the signal. The mathematical expression of the frequency pulse depends on the selected waveform. Table 1 shows the frequency response for the tested CPM schemes, with $\mathrm{Q}(\cdot)$, the Gaussian error function. It is important to note that, in this table, B denotes the 3 dB bandwidth of the filter,

while T_s is the duration of one input data symbol, BT_s is usually called *Bandwidth-Time product*.

TABLE 1. CPM pulse shape.

Name	Frequency pulse	Support	Parameters
RC	$g(t) = \frac{1}{2LT_s}(1 - \cos(\frac{2\pi t}{LT_s}))$	$[0, LT_s]$	L
GMSK	$g(t) = \frac{1}{LT_s}\{Q(2\pi B\frac{t-T_s/2}{\sqrt{(\ln(2))}}) - Q(2\pi B\frac{t+T_s/2}{\sqrt{(\ln(2))}})\}$	Infinite	L, BT_s

III. PHOTODIODE NON-LINEARITIES

A. A MATHEMATICAL MODEL ON NON-LINEARITIES

Photodiodes present non-linear behavior; their output amplitude and phase have a saturation point, after which its using is at risk of breaking [24]. The literature presents numerous schemes and performance of photodiode, however the non-linear amplitude-to-amplitude (AM-AM) and amplitude-to-phase (AM-PM) behavior remains [24], [25], [26], [27], [28], [29], [30], [31], [32], [33], [34], and [35]. Due to the difficulties of measuring the non-linearities of photodiodes, typical AM-AM and AM-PM behavior figures was extracted from the literatures [25], [35]. The non-linear AM-AM and AM-PM behavior of photodiodes is similar to the non-linear AM-AM and AM-PM behavior of traveling-wave tubes and power amplifier used in satellite communications [36]:

$$\begin{cases} A(r) = \dfrac{\alpha_a r}{1 + \beta_a r^2} \\ \Phi(r) = \dfrac{\alpha_\Phi r^2}{1 + \beta_\Phi r^2}, \end{cases} \tag{3}$$

with, $A(r)$ and $\Phi(r)$ the AM-AM and AM-PM transfer functions respectively, r the complex modulus of the input signal, and α and β the parameters of the model. This model was used as a baseline to obtain the AM-AM and AM-PM NL-PD (Non-Linearity - PhotoDiode) model proposed in this paper.

From this baseline and the gathered data from the literature, and by using the Levenberg-Marquardt technique, also known as the damped least-squares method, which is used to solve non-linear least square problems [37], [38], used jointly with the addition of higher order terms, the AM-AM, eq. (4) and AM-PM, eq. (5), transfer functions were mathematically modeled:

$$\mathrm{F_{AM\text{-}AM}}(t) = \left(\frac{g \cdot |x(t)|}{1 + a \cdot |x(t)| + b \cdot |x(t)|^2 + c \cdot |x(t)|^3}\right)^2, \tag{4}$$

$$\mathrm{F_{AM\text{-}PM}}(t) = \frac{a + b \cdot |x(t)| + c \cdot |x(t)|^2}{d + e \cdot |x(t)| + f \cdot |x(t)|^2}, \tag{5}$$

with a, b, c, d, e, f, and g real values independent from one model to the other, $x(t)$ is the signal at the input of the photodiode, while $|.|$ denotes the complex modulus, and $\mathrm{F_{AM\text{-}AM}}(t)$ and $\mathrm{F_{AM\text{-}PM}}(t)$ the AM-AM and AM-PM transfer function respectively. The AM-AM and AM-PM combined transfer function is given by:

$$y(t) = \mathrm{F_{AM\text{-}AM}}(t) \cdot e^{(\mathrm{Arg}\{x(t)\} + \mathrm{F_{AM\text{-}PM}}(t))}, \tag{6}$$

with $y(t)$ the signal at the output of the photodiode. Fig. 2 shows the simulations of the equation (6) with the AM-AM and AM-PM models. The lines with circle markers are for AM-to-AM measures, while the lines with star markers are for AM-to-PM measures. The numerical values used to obtain these curves are presented in Appendix. The α, β, γ and δ over the curves are written on the figure to differentiate the four presented cases.

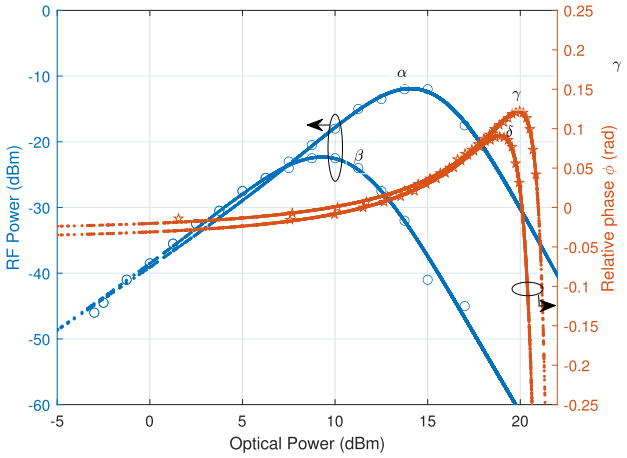

FIGURE 2. AM-to-AM and AM-to-PM transfer curves with data from [25] and [35] and using the model in eq. (6): (α) $V_{bias} = -1.2$ V, (β) $V_{bias} = -0.2$ V, (γ) $V_{bias} = -5$ V, (δ) $V_{bias} = -4$ V.

The AM-AM saturation power is linked to the bias voltage applied to the photodiode. This bias voltage affects the linearity of the photodiode, a reversely high bias voltage reduces the capacitance of the photodiode, which pushes higher the saturation point [39]. This explains why, with $V_{bias} = -1.2\ V$, the saturation point is higher than with $V_{bias} = -0.2\ V$.

Figure 3 gives an illustrative example on the modeling of NL-PD affecting filtered QPSK and CPM signals.

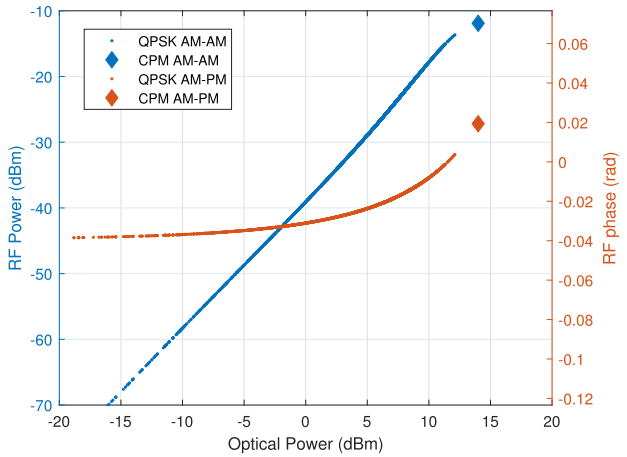

FIGURE 3. AM-AM and AM-PM figures of: (a) QPSK signals, and (b) CPM signals.

This figure was obtained for a filtered QPSK with a back-off high enough as to not suffer from non-linear effects

in the AM-AM domain. In the AM-PM domain however, there are still non-linearities that affects the signal, though they are small enough to be neglected in this case (from −0.04 rad to 0 rad). This figure also shows the constant modulus property of the CPM waveform, which allows the use of the photodiode at saturation.

B. PERFORMANCE DEGRADATION DUE TO NON-LINEARITIES

To study the effects of photodiodes non-linearities (NL) on communication signals, an uncoded, baseband, Single-Input Single-Output (SISO) system with Additive White Gaussian Noise (AWGN) channel including photodiodes non-linearities at the transmitter was considered. The received signal is defined as:

$$r(t) = y(t) + n(t), \tag{7}$$

with $r(t)$ the received signal, $y(t)$ the signal at the output of the photodiode, affected by NL using the model described in (6), and $n(t)$ the circular, zero-mean, complex white Gaussian noise with variance σ^2. The transmitted signal is composed of filtered symbols that take their values from the following modulations: QPSK, 16-QAM, GMSK, and RC. A Square-Root Raised Cosine (SRRC) with a roll-off factor of 0.2 filter was designed for the M-QAM symbols, while CPM is used with binary antipodal symbols, with GMSK ($h = 1/2$, $L = 4$ & $BT = 0.3$) or RC ($h = 4/5$, $L = 3$) pulse shaping.

To observe the effects of NL, a focus is done on calculating the Adjacent Channel Power Ratio (ACPR), Bit Error Rate (BER), and Error Vector Magnitudes (EVM). Due to the continuous phase and memory effects of the CPMs, it is unsuitable to talk about the EVM as a performance metric; for instance, only BER and ACPR will be shown for these signals. ACPR is calculated by comparing the first channel offset with the in-band power. BER values were calculated for values of E_b/N_0 from −5 to 15 dB and compared with their respective theoretical lower bounds.

The α and δ NL curves from Fig. 2 were used in our simulation setup. Applying a power back-off to the signal before the photodiode is necessary to account for the NL effects. The applied power back-off should be strong enough to keep the signals in the linear zone. The maximum instantaneous input power must be lower than 12 dBm for M-QAM signals, whereas the input power was fixed at saturation (14 dBm) for the CPM signals, as shown in Fig. 3.

Another way to explain this is by using the Peak-to-Average Power Ratio (PAPR) of the modulations. The PAPR shows the higher bound of the instantaneous variations of the signal power. The mean E[·] input signal power P_{in} in a photodiode must be lower or equal to the saturation point P_{sat} minus the PAPR:

$$\mathrm{E}[P_{in}] \leq P_{sat} - \mathrm{PAPR}. \tag{8}$$

Table 2 gives the PAPR values of the considered waveforms.

TABLE 2. PAPR table of considered waveforms.

Waveform	QPSK	16-QAM	RC	GMSK
PAPR (dB)	5	6	0	0

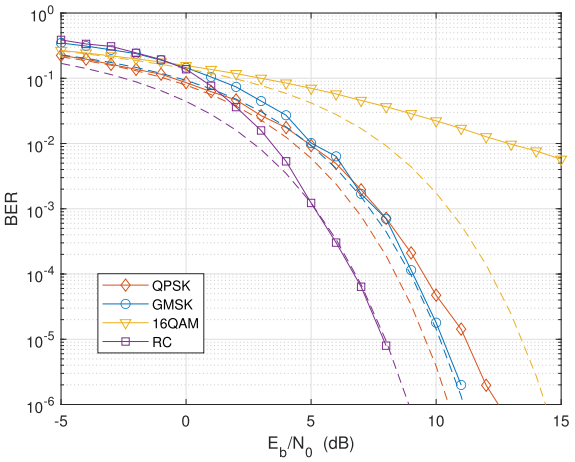

FIGURE 4. Bit error rate degradation due to photodiode non-linearities.

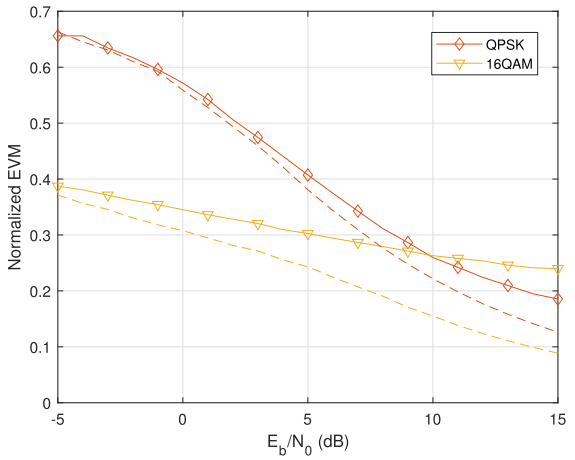

FIGURE 5. Error vector magnitude degradation due to photodiode non-linearities.

Fig. 4 shows the simulated BER curves of the considered system, while Fig. 5 shows the normalized EVM curves. In both figures, the solid lines show the simulated curves with non-linearities. On the other hand, the dashed curves present the theoretical lower bound (BER) or the simulated system without non-linearities (EVM). As expected, the BER of both CPM are unaffected by the non-linear effects of the photodiodes, while the QPSK shows low degradation at high E_b/N_0 (3 dB for a BER of 10^{-5}) and 16-QAM presents high degradation at medium to high E_b/N_0 ($\sim$ 5 dB for a BER of 10^{-2}). The EVM shows similar effects: low degradation at high E_b/N_0 for the QPSK, while 16-QAM suffers from high degradation at medium to high E_b/N_0.

Fig. 6 shows the Power Spectral Densities (PSD) of the waveforms with 6(b) and without 6(a) non-linear effects. In these two illustrations, the mean in-band power is −12 dB, while the power in the adjacent channel differs from one

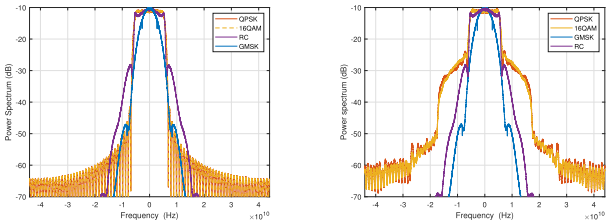

(a) (b)

FIGURE 6. Power Spectral Densities of: (a) no non-linear effects, and (b) photodiode non-linear effects.

illustration to the other. In the case of M-QAM, there is a higher power in the adjacent channel with non-linearities than without, and the ACPR here is increased by 27 dB. On the other hand, the PSD of both CPM waveforms do not show any increase in their ACPR.

To conclude, and by using the BER, EVM, and ACPR degradation analysis, the CPM waveform does not present any degradation due to non-linear effects. Meanwhile, M-QAM waveforms present degradation and their level depends on the order of the modulation. The higher the order, the higher the degradation. Except for the ACPR, which depends on the pulse shaping filter, the SRRC with 0.2 roll-off pulse shaping shows an increase of 27 dB in the ACPR.

This effect on the ACPR is due to intermodulation distortions induced by the non-linear behavior of the photodiodes [29], [39], [40]. These distortions affect time-dependent parameters such as the amplitude and phase of the signals. The constant modulus of CPM waveforms gives them extreme robustness against such effects, which enables the use of photodiodes and other non-linear equipment at their saturation point.

C. COMMUNICATION RANGE GAIN

In this study, the BER is derived within a specified communication range. These findings unveil new avenues for wireless photonics-based communications facilitated using CPM waveforms. Supposing an AWGN channel as described in equation (7), and by fixing a target BER, it is possible to compute the theoretical E_b/N_0 required to achieve a pre-fixed target BER:

$$\frac{E_b}{N_0}|_{\text{M-QAM}} = 10 \cdot \log_{10} \left(\frac{2}{3} \cdot \frac{M-1}{\log_2(M)} \cdot \text{erfc}^{-1} \left(\text{BER} \cdot \frac{\log_2(M)}{2(1-\frac{1}{\sqrt{M}})} \right)^2 \right) \tag{9}$$

$$\frac{E_b}{N_0}|_{\text{CPM}} = 10 \cdot \log_{10} \left(\frac{2}{d_{min}^2} \cdot \text{erfc}^{-1}(2 \cdot \text{BER})^2 \right) \tag{10}$$

with erfc^{-1} the inverse function of the complementary error function, BER the targeted BER, M the order of the QAM modulation, and d_{min}^2 the minimum normalized squared Euclidean distance in the signal space [23]. From this E_b/N_0 value, and by knowing the system bandwidth and the data rate of the communication signal, it is possible to calculate the minimum Signal-to-Noise Ratio (SNR) required to achieve the targeted BER:

$$\text{SNR} = \frac{E_b}{N_0} + 10 \cdot \log_{10}(R_b) + 10 \cdot \log_{10}(B_s), \tag{11}$$

with R_b the data rate in bits/s and B_s the system bandwidth in Hz. From this SNR, it is possible to calculate the theoretical power threshold at the receiver to enable correct detection of the information:

$$S_p|_{\text{dB}} = (N_0 + \text{NF}_{\text{system}} + \text{SNR}), \tag{12}$$

with N_0 the thermal noise level at the receiver, $\text{NF}_{\text{system}}$ the global noise figure of the analog system used at the receiver, SNR the calculated theoretical SNR. The thermal noise power at the receiver was calculated by using the equation $N_0 = 10 \cdot \log_{10}(K_B B_s T)$, with K_B the Boltzmann constant, B_s the system bandwidth (Hz) and T the system temperature (K).

By processing the link budget for varying distances, a minimum distance at which the minimum instantaneous received power is higher than the calculated threshold S_p is found. This minimum instantaneous power is estimated, such as 99% of the power of the signal being higher. The distance is considered here as the maximum range for which the targeted BER is achieved.

The theoretical SNR was calculated using the parameters, which are linked to the experimental setup shown in Fig. 12, and to the propagation model presented in table 3. At the same time, the parameters presented in table 4 are used to calculate the theoretical threshold defined in (12). As for the photodiode NL, they were simulated by using the model presented in (6), with the parameters leading to the α and δ curves in Fig. 2. A power back-off is applied to the M-QAM signals to keep their instantaneous powers in the linear region of the AM-AM model described in (4), while CPM signals are used at saturation. As shown previously, the CPM waveforms are robust against such NL, thus allowing their use at saturation.

To account for the randomness of the instantaneous received power of the communication signals, Monte-Carlo integration techniques were used with 1000 iterations.

Fig. 7 shows the Complementary Cumulative Distribution Function (CCDF) of the maximum communication range for communication signals impaired by photodiode NL, with a target BER of 10^{-3}, which is low enough to enable the use of high-performance FEC algorithms such as LDPC or Turbo-codes. This figure shows the probability of receiving the signal given a certain threshold. All 16-QAM signals are received for distances less than or equal to 26 meters, while this distance becomes 149 meters for QPSK signals. Compared to CPM waveforms, for which this distance becomes 2382 meters for GMSK and 2978 meters for RC, CPM waveforms allow a much higher communication range, mainly due to their robustness to nonlinear effects.

TABLE 3. Photonic-wireless sub-THz link budget.

Parameters							
	Temperature (K)	290	Carrier frequency (GHz)		107.5	Distance (m)	[1,3000]
	System bandwidth (GHz)			20	Water vapor concentration (g/m^3)		7.5
System				Channel			
Tx		Rx		Propagation		Noise	
Photodiode input power	$E[P_{in}]$	Antenna gain	36 dBi	Attenuation	CI model [41]–[43]	Thermal noise	-68.04 dBm
		LNA gain	29.5 dB			Noise figure	2.4 dB
Photodiode power loss	-38.5 dB	Cable losses	1 dB	Gas	-0.53 dB/km	Total noise	f(Distance)
Coupling losses	3 dB	Rx mixer losses	6 dB				
Antenna gain	37 dBi	Connection losses	2 dB	Total	f(Distance)	SNR	f(Distance)
		Received power	f(Distance)				

TABLE 4. Waveform parameter for range calculations.

Waveform	QPSK	16-QAM	RC	GMSK
d^2_{min}	-	-	2.9	1.75
R_b (Gbps)	18.3	36.7	11	11

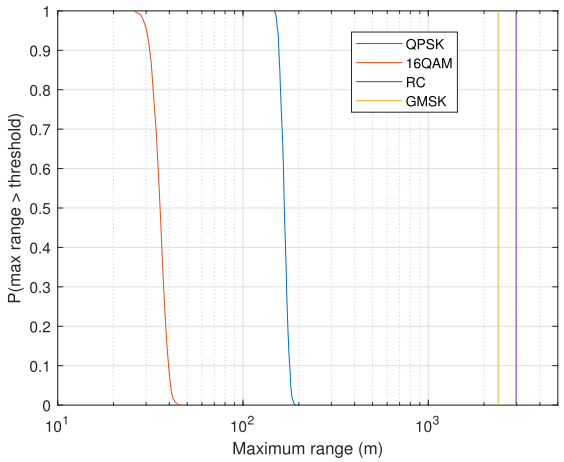

FIGURE 7. Complementary cumulative distribution function of the maximum range for communications impaired by photodiode NL with target BER = 10^{-3}.

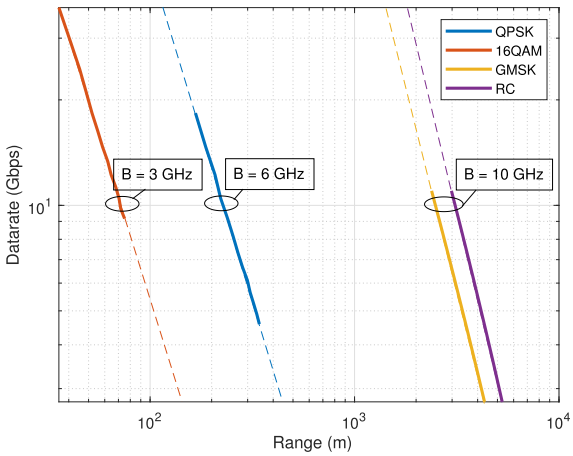

FIGURE 8. Data rate versus maximum range for communications impaired by photodiode NL with target BER = 10^{-3}.

Fig. 8 shows the theoretical data rate versus the calculated distance in a log-log scale for a target BER of 10^{-3}. The dashed lines are extrapolated from the solid lines. The achievable data rate varies logarithmically with the distance. For the same rate of 10 Gbps, with 16-QAM, one can communicate at a distance of 71 meters, which becomes 225 meters for QPSK, 2500 meters for GMSK, and 3100 meters for RC. The figure also indicates the bandwidth required to achieve this data rate, from 3 GHz for the 16-QAM to 6 GHz for the QPSK and 10 GHz for both CPM. Thus, this figure illustrates well the trade-off bandwidth versus communication range. It might be better to choose M-QAM modulations in a heavily bandwidth-constrained communications scheme. Meanwhile, when bandwidth is not the primary concern in a long-range application, CPM is the family of waveforms to choose from.

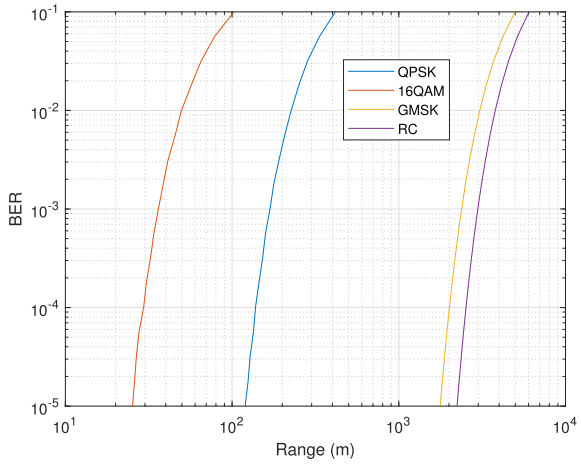

FIGURE 9. BER versus maximum range for communications impaired by photodiode NL with R_b taken from table 8.

Fig. 9 outlines the BER achieved as a function of the maximum communication range, averaged over the number of Monte-Carlo iterations, for the data rates exposed in table 4. In this case, the bandwidth is the same for each presented waveform. This figure presents another trade-off: uncoded error performance versus communication range. Looking at this figure only, the trade-off becomes clear: CPM gives the best uncoded error performance. Now, considering the trade-off between bandwidth and range, the selection of one waveform over another becomes a strategic decision contingent upon the specific requirements of the application.

Continuing from the exploration of performance metrics guiding waveform selection in the preceding section, the focus is shifted to introduce a new dimension in our trade-off dilemma: energy efficiency.

IV. ENERGY EFFICIENCY

Energy consumption and greenhouse gas emissions are major concerns in today's world. The potential of communication technology has been thoroughly studied by Andrae and Edler [44]. This study shows that, by 2030, communication technology could be responsible for up to 23% of global greenhouse gas emissions in the worst-case scenario. Future communication systems should be aware of this and integrate high energy efficiency schemes modes. To pursue this aim, a straightforward model to express the energy efficiency of wireless communication systems comes [45], [46], [47]:

$$\eta_e = \frac{\eta_s}{\frac{P_c}{B} + (2^{\eta_s} - 1)\frac{N}{G_t}}, \tag{13}$$

with η_e the Energy Efficiency (EE), η_s the Spectral Efficiency (SE), $N = K_B \cdot T$ the thermal noise power at the receiver, G_t the total channel gain, B the system bandwidth, and P_c the power consumed by the analog circuits and the digital processing chain. P_c can also be described as the base level of power needed to operate the system [45]. From the equation of the signal propagation in [48] and [49], the path-loss is obtained:

$$L = \frac{D^n}{k}, \tag{14}$$

with D the communication range, $k = \frac{1}{\mathrm{PL}_0 \cdot \chi}$ losses due to the reference losses at 1 m (PL_0) and shadow fading (χ), and n the path-loss exponent. The total channel gain can be expressed as:

$$G_{tot} = \frac{G_t \cdot G_r \cdot G_{LNA}}{L_{PD} \cdot L_{elec} \cdot L_{atm}} \tag{15}$$

with G_t the transmitting antenna gain, G_r the receiving antenna gain, G_{LNA} the LNA gain, L_{PD} the conversion power loss due to the photodiode, L_{elec} the electrical losses in the transmitter and receiver, and L_{atm} the atmospheric gas absorption [50].

Knowing equations (14) and (15), (13) becomes:

$$\eta_e = \frac{\eta_s}{\frac{\alpha \cdot P_n \cdot (2^{\eta_s} - 1) \cdot D^n}{G_{tot} \cdot k} + \frac{P_c}{B}}, \tag{16}$$

with $P_n = N \cdot \mathrm{NF}_{\mathrm{system}}$ the power of the noise after the Low Noise Amplifier (LNA) at the receiver, $\mathrm{NF}_{\mathrm{system}}$ the noise figure of the global analog system, and α the power back-off applied to the signal to keep it in the linear regime of the photodiode. α is determined with regard to the AM-AM saturation point of the photodiode. This model shows the EE vs SE in a SISO communication scheme without any consideration of waveform.

Fig. 10 was obtained considering the same setup as previously, with a 10 dB power back-off (dashed curves) and without power back-off (solid curves), for distances corresponding to the results obtained from our non-linear study: from 26 to 2978 meters. For comparison purpose, a circuit power consumption of 25 dBm and photodiode power conversion losses equal to 38.5 dB are considered. This corresponds to the output power at 0 dBm of input power in the AM-AM curves of Fig. 2.

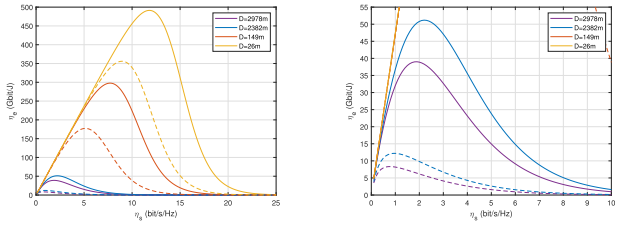

(a) (b)

FIGURE 10. Energy efficiency vs spectral efficiency at varying distances, without power back-off (solid curves) and with $\alpha = 10$ dB power back-off (dashed curves). (a) shows the overall figure while (b) shows a zoomed-in figure towards the long range communication cases.

This figure shows concave curves, with, at their maximum, the optimal trade-off between EE and SE. EE is represented by the amount of data (in Gbits here) per unit of energy (J) the link can support, while SE is expressed in bits/s/Hz. One expected result is that the longer the distance, the lower the optimal trade-off in EE and SE. Using a power back-off to keep the signal in the linear regime decreases the optimal trade-off. It comes from the fact that the devices are not used at their maximum power output, thus resulting in a loss of energy efficiency.

CPM waveforms demonstrate exceptional performance in long-distance communication scenarios; using a CPM waveform, such as RC or GMSK, allows the use of the photodiode at its AM-AM saturation point, without losing in BER and ACPR performance as shown by Fig. 4 & 6b. For this case, at 2978 meters, the optimal SE becomes 1.9 bits/s/Hz. M-ary CPM could allow such SE performance while keeping EE higher than M-ary linear waveforms.

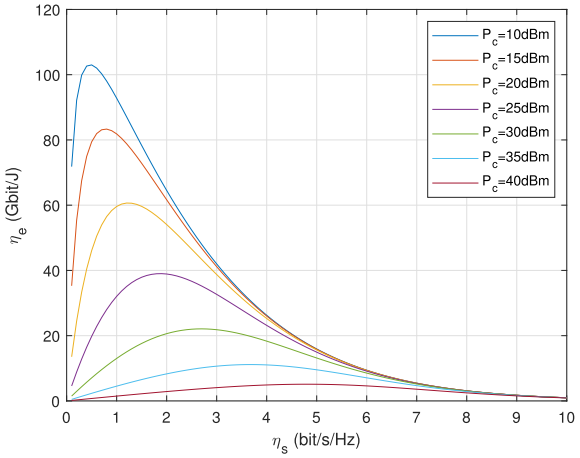

FIGURE 11. Energy efficiency vs spectral efficiency at 2978 m, without power back-off, and with different circuit power.

This particular case of a communication range fixed at 2978 meters corresponds to the use case of RC waveform at 10^{-3} of BER. Fig. 11 shows the trade-off EE vs SE depending on the circuit power consumption. The optimal trade-off between EE and SE decreases in EE but increases in SE, which means that to stay optimal regarding the EE-SE trade-off, the more one consumes power in the circuitry of their system, the higher the modulation order should be. From another side, this figure supports the idea that if one wants to save energy, *i.e.* by consuming less in the circuitry, the EE becomes optimal for low-order modulations, such as CPM.

While P_c is the base power consumption of the system, P_t is the added power when transmitting. In a low-consumption system, low-order modulations should be used to maintain low power consumption, thus achieving optimality in EE. Contrary to that, in a high-consumption system, a higher order of modulations should be used to achieve optimality in EE.

V. SUB-THZ EXPERIMENTATIONS

A. EXPERIMENTAL SETUP

Fig. 12 presents our experimental setup. The analog signal is generated by an Arbitrary Waveform Generator (AWG) with 88 GSps of sample rate, 25 GHz of bandwidth and 2^{14} samples of memory length. One of the optical wavelengths (λ_1), obtained from an External Cavity Laser (ECL), is modulated by the output of the AWG thanks to an electro-optical IQ modulator. The analog signal delivered by the AWG consists of a waveform designed in the digital domain, detailed in Table 5. A second ECL delivers the reference (λ_2) for the carrier frequency generation. The difference between the two lasers frequency gives the reference ($\Delta_f = F_{ECL_2} - F_{ECL_1}$), in these experiments, $\Delta_f = 107.5$ GHz. The power imbalance of the two signals is approximately offset by the 90/10 optical coupler and finely adjusted by adapting the pump current of each ECL. One percent of the signal is extracted to monitor the power spectrum, while the remaining 99% are amplified by an Erbium-Doped Fiber Amplifier (EDFA). An attenuator is then used to monitor and adapt the power of the signal. Then, the optical signal is transmitted to a commercial TOPTICA photomixing emitter. This transmitter consists of an ultra-broadband P-i-N photodiode connected to a lens-integrated bow-tie antenna [51]. This antenna is placed at the focus of a larger Teflon lens.

Correspondingly, at the receiver side, a W-band horn antenna is placed at the focus of a second Teflon lens to capture the radiated power. A rectangular waveguide of bandwidth [75-110] GHz is connected to the output of the horn antenna. The output of this waveguide is linked to a Sub-Harmonic Mixer (SHM), fed by a Local Oscillator (LO), generating a 50 GHz tone. Thus, the received signal is transposed to an Intermediate Frequency (IF) of 7.5 GHz. The IF signal is then amplified by a Low-Noise Amplifier (LNA). The output signal of the LNA is acquired with an oscilloscope working at 100 GSps with an analog bandwidth of 33 GHz. Finally, the acquisitions are treated offline.

The experiment was constrained to a short wireless point-to-point link, ranging from 0.2 m to 1.8 m, due to the low available space in the laboratory. Due to the availability of the photonic and electronics components the experiment was also constrained to SISO communications.

TABLE 5. Parameters of the waveforms used in experiments.

Waveform	Parameters	Bandwidth (GHz)	Spectral efficiency (bit/s/Hz)	Net bitrate (Gbits/s)
RC	$h = \frac{4}{5}, L = 3$	7.75	0.95	7.36
GMSK	$h = \frac{1}{2}, L = 4, BT = 0.3$	8	0.96	7.68
QPSK	SRRC of 0.2 roll-off factor	8	1.92	15.36

The GMSK parameters are the same as the waveform used in the second generation of mobile communications. The RC parameters are chosen to compromise detection performance and complexity at the receiver [23], [52], [53]. In both CPM schemes, binary antipodal symbols were used, which corresponds to the $\alpha_i \in \{-1, +1\}$ symbols from equation (1).

The main goal of these experiments is to produce an experimental proof of concept of a photonics-based sub-THz wireless transmission using large bandwidth CPM waveforms and to compare them with filtered QPSK signals. 16-QAM signals were used as well during these experiments. However, the performance obtained from the 16-QAM signals were not up to the standard, they are not included in the results sections.

It is worth noting that no Forward Error Coding (FEC) were used during these experiments.

B. MEASUREMENTS AT FIXED SNR

The measurement procedure was as follows: first, the waveform was designed in the digital domain before being played by the AWG. The signal from the AWG modulated an optical carrier, which was then combined with an optical tone at the frequency $F_{ECL_2} = F_{ECL_1} + \Delta_f$. The Radio-Frequency (RF) signal at the output of the photodiode was sent to the wireless link and then received by the horn antenna. This RF signal was finally transposed to IF, amplified, and acquired on an oscilloscope. The data acquired was then treated offline by a custom-made software.

Using the same parameters as presented in table 3, the expected link budget is calculated using the Close-In (CI) model which has been used to model directional path-loss in the sub-THz context [41], [42], [43]:

$$L_{dB} = \mathrm{FSPL}(d_0, f) + 10\, n \log_{10}(d/d_0) + \chi, \qquad (17)$$

with L_{dB} the path-loss in dB, d the communication distance with d_0 its reference, f the carrier frequency, n the path-loss exponent and χ the shadow fading. The $\mathrm{FSPL}(d_0, f)$ term refers to *Free-Space Path-Loss* and is expressed by $32.4 + 20\log_{10}(f) + 20\log_{10}(d_0)$ dB. From this path loss, and the

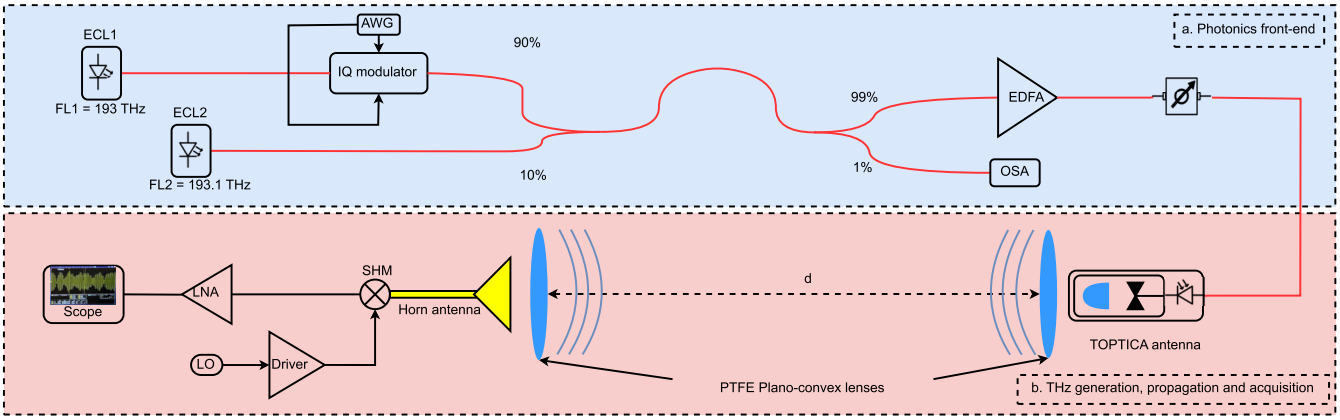

FIGURE 12. Experimental setup for Sub-THz wireless transmission of baseband selected waveforms. a. depicts the photonic front-end of the transmitter, while b. shows the sub-THz wave generation, propagation, and acquisition on a 100 GSps scope. AWG: Arbitrary Waveform Generator, IQ modulator: In-phase and Quadrature baseband modulator, OSA: Optical Spectrum Analyzer, EDFA: Erbium-Doped Fiber Amplifier, PTFE: Polytetrafluoroethylene, ECL: External Cavity Laser, SHM: Sub-Harmonic Mixer, d: wireless communication distance.

equation (15), the overall sub-THz link budget becomes:

$$P_{Rx,dB} = P_{Tx,dB} + G_{t,dB} + G_{r,dB} + G_{LNA,dB} - L_{PD,dB} - L_{elec,dB} - L_{atm,dB}, \quad (18)$$

with $P_{Tx,dB}$ and $P_{Rx,dB}$ the optical power before photodiode and received power after LNA respectively.

Using a distance of 1 m as a reference, a path-loss exponent of $n = 1.7$ [42], a shadow fading of $\chi = 0.7$ dB [42] and a carrier frequency of 107.5 GHz, the propagation losses were calculated to be 73.7 dB. The thermal noise power at the receiver was obtained by using the equation $n = K_B BT$, with n the noise power (W), K_B the Boltzmann constant, B the system bandwidth (Hz) and T the system temperature (K). Considering power losses of -27.3 dB from our photodiode and a optical power of $P_{Tx} = 10$ dBm at its input, the SNR at the receiver side is calculated to be 68.04 dB after the LNA. The system noise figure was considered to be NF $= 2.4$ dB. Before LNA, the SNR is calculated at 41.94 dB. Based on the Signal to Quantization-and-Noise Ratio (SQNR) expression, given by 19 [54]. As the receiver is using a 6-bit effective quantization, the SQNR of the link is 37.88 dB.

$$\text{SQNR} \simeq 6.02\, n + 1.76, \quad (19)$$

with SQNR, the Signal to Quantization-and-Noise Ratio in dB, and n, the number of effective quantization bits. This SQNR is a maximum value, upper bounding the achievable SNR.

Experimentally, an SNR between 17 and 23 dB is measured after quantization and acquisition on an oscilloscope. Non-ideal experimental conditions, and more specifically, misalignment losses due to difficult antenna alignment [55], as well as non-thermal noise (shot noise, spontaneous flutter, and scintillation noise) due to photonic and electronic equipment [40], [56], decrease the overall SNR of the communication. The weather is also to be considered here, as the temperature in the laboratory was high (measurements taken in June 2023). The ambient water vapor concentration was high (measurements taken in Brittany, France, where in June 2023, the local weather office indicated an average humidity of 60% and a maximum of 99%), as well as the atmospheric pressure (1017.4 hPa). All of this explains why SNR measurements are so low compared with their theoretical values.

Fig. 13 shows the PSD of the acquired signals. In the bandwidth of the signal, a saw-like degradation is observed. Due to a cavity effect inside the package of the transmit antenna, some frequencies are amplified while others are significantly attenuated, which gives this saw-like pattern. The performance of the transmission is consequently highly affected. The out-of-band, saw-like effect in the PSD of the GMSK is mainly due to a temporary malfunction of the IQ modulator.

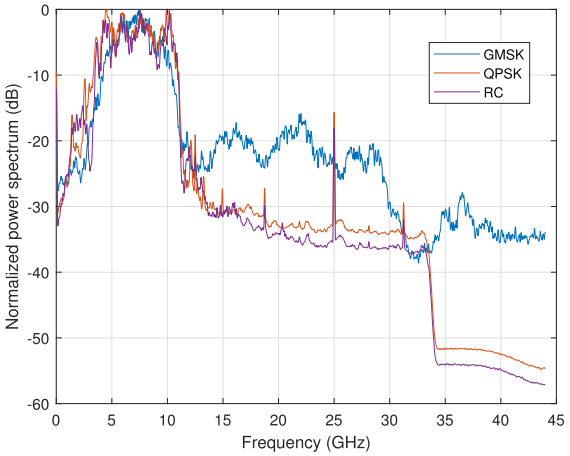

FIGURE 13. Normalized PSD of observed waveforms at IF = 7.5 GHz after acquisition on a 33 GHz scope.

Table 6 sums up the results, with nBits the number of received bits, BER the Bit Error Rate calculated, EVM the Error Vector Magnitude calculated, and SNR the Signal to Noise Ratio. The SNR was calculated from the PSDs, by calculating the in-band mean power and comparing it to

the out-of-band mean power. Due to the continuous phase and memory effects of the CPMs, it is unsuitable to talk about the EVM as a performance metric. Consequently, only the BER will be used as a comparison metric. Each numerical value in Table 6 is averaged over five independent measurements.

TABLE 6. Results obtained from analysis of THz communication scheme.

Waveform	Symbol rate (Gbauds)	nBits	BER	EVM	SNR (dB)
RC	7.5	$5.28 \cdot 10^5$	$< 1.8939 \cdot 10^{-6}$	-	22.6
GMSK	7.5	$1.56 \cdot 10^6$	$< 6.4103 \cdot 10^{-7}$	-	17.2
QPSK	7.5	$5.60 \cdot 10^5$	$< 1.7857 \cdot 10^{-6}$	0.173	22.3

To analyze these results, the number of bits received must be remembered. In this case, *quasi-error-free* communications was measured; the average BER of the experimental link is lower than 1/nBits, which is $1.8939 \cdot 10^{-6}$ for RC, $6.4103 \cdot 10^{-7}$ for GMSK, and $1.7857 \cdot 10^{-6}$ for QPSK. In this case, the BER of RC is similar to that of the QPSK, while it is much lower for the GMSK signals. However, here, QPSK presents a much larger data rate than CPM signals.

C. SIMULATIONS AT DIFFERENT SNR VALUES

Before going any further, it is crucial to understand that previously, the results of experiments at a single SNR value was shown, due to the fixed communication distance. To go further with these results, White Gaussian Noise (WGN) is numerically added to the received signals. Allowing to plot the BER curves depicted in Fig. 14. All 5 measurements of each waveform gave similar BER vs E_b/N_0 performance. Thus, one measure of each waveform was selected and plotted in Fig. 14. The added noise was calculated with respect to the bit power (E_b/N_0) in dB. These BER curves present a simulation of what might have happened if the experiments had been conducted at different distances or transmitting powers.

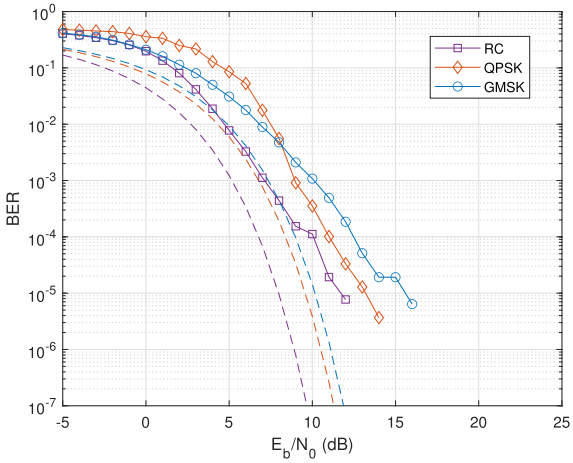

FIGURE 14. BER curves for added Gaussian Noise to observed data. Plain lines denote measurements, while dotted lines show the theoretical AWGN lower bound.

The three presented waveforms have their BER curves close to their uncoded AWGN lower bounds, with a 4 to 5 dB difference at high E_b/N_0. Such results show that, at longer distances or lower transmission power, and considering the same propagation channel, the uncoded BER is close to its lower bound.

Considering the reported experimental setup, with a transmitting antenna showing saw-like patterns in the signal spectrum, and knowing malfunctions happened during the measurements, these results should be treated cautiously. They can be significantly improved but that is not the aim of this study: the feasibility of a photonic-wireless sub-THz link with CPM waveforms is shown.

These results presented here are a significantly improved version of the results reported in the previous work [21]: better BER, addition of RC waveform and comparison with QPSK, and finally, higher data rates.

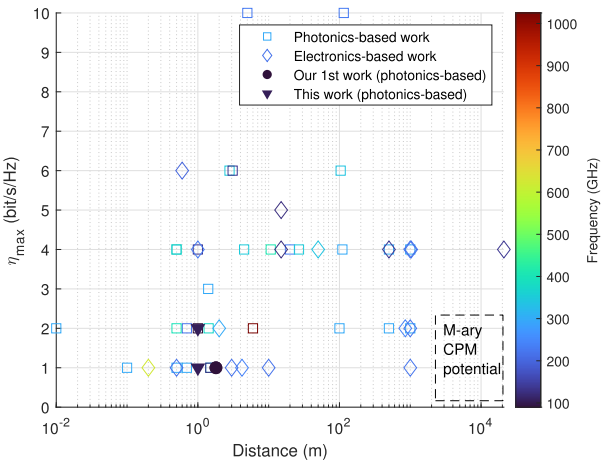

FIGURE 15. Sub-THz communications state-of-the-art, with CPM opening.

Based on the analysis of non-linearity and energy efficiency, as well as the findings from the experiments, it is evident that the use of CPM waveforms holds significant promise to facilitates long-range wireless-photonic Sub-THz communications. The emergence of this newly accessible long-range application is illustrated in Fig. 15.

VI. DISCUSSION ON FUTURE RESEARCH AND PRACTICAL USE

In the sub-THz context, several applications are considered for next generations of communications: inter-chip communications [57], [58], inter-datacenter communications [4], [58], [59], [60], kiosk downloading [4], [57], [58], hotspot communications [61], vehicle-to-everything [4], [62], [63], and wireless backhaul networks [4], [57], [58], [61], [62], [64]. Out of all these scenarios, wireless backhaul networks are of particular interest for CPM: long-range communications, with tens of Gbits/s of data rate. In other scenarios, such as inter-chip communications, were the range is extremely short, high-order linear modulations such as 64-QAM might be preferred over the use of CPM.

On the other hand, using CPM waveforms comes with a higher complexity at the receiver. The use of the Viterbi algorithm to detect the information implies a high calculation complexity [23]. By using the Laurent decomposition, this

complexity can be significantly reduced [65]. Mengali and Morelli extended the Laurent decomposition to M-ary CPM signals [66]. In systems using CPM waveforms, using reduced complexity receivers enables high performance while keeping BER degradation low [53], [67], [68].

Another downside of the proposed physical layer is the lower achievable data rate compared with linear modulations such as M-QAM. However, by using Multiple-Input Multiple-Output (MIMO) techniques combined with indexing on the spatial domain (Generalized Spacial Modulation), it is possible to significantly increase the data rate of the proposed scheme [69], [70]. However, these techniques add hardware complexity to the system as there is a need for a high number of analog chains and antennas to enable generalized spatial modulation [70], [71], [72], [73]. Another significant challenge in hardware complexity is also the design of efficient digital-to-analog and analog-to-digital converters that enable sub-THz communications [64].

One of the main results this paper reports is the communication range gained by using CPM waveforms against conventional M-ary QAM modulations. In a simple photonic-wireless SISO scheme, with a signal bandwidth of 11 GHz and a target BER of 10^{-3}, the proposed CPM scheme enables communications up to 2978 meters. Meanwhile, QPSK, in the same context, enables communications up to 149 meters.

One of the considered future works is quantifying the communication range gained using CPM in a photonic-wireless sub-THz MIMO system with generalized spatial modulation to increase data rates. This theoretical study can be conducted jointly with the scalability of the proposed solution, as this is still an open problem for sub-THz and THz communications [74]. The second considered work is to push further the experiments: short-range indoor, long-range indoor, short-range outdoor, long-range outdoor, and very long-range outdoor line-of-sight communications. These scenarios would be designed to test the limitations of the proposed techniques.

VII. CONCLUSION

This work carries the perspective of a long range, high data rate, low energy consumption for sub-THz communications enabled by photonics technologies. It proposes an energy-efficient, robust against non-linear effects, alternative to the state-of-the-art of sub-THz communications.

A mathematical model is proposed to numerically simulate photodiode non-linearities effects on a given communication signal. Then, said model is used to simulate a communication chain impaired by non-linearities due to photodiodes and compare linear waveforms (QPSK & 16-QAM) with CPM waveforms (GMSK & RC). It shows that, in general, CPM waveforms are extremely robust against such non-linear effects. CPM can operate at saturation whereas linear waveforms need a power back-off to stay in the linear region. Then, this model is used to find out the farthest communication distance achieved for a fixed targeted BER. This distance is shown to be near 20 times higher for the chosen RC scheme than for the filtered QPSK.

Then, insights on energy efficiency and power consumption are given. Using a modified energy efficiency vs spectral efficiency model, the appeal on the use of CPM to help to optimize the global energy consumption of future communications systems is presented.

Finally, it was experimentally shown that CPM waveforms are working candidates for sub-THz communications. This was done by setting up a photonics-based wireless sub-THz link at 107.5 GHz carrier frequency. Without using FEC algorithms, error-free transmissions were achieved with 7.5 GBauds RC, GMSK & QPSK signals at a 1m distance.

In a wireless, long-range, photonic-enabled communication link, the CPM waveform could be a good candidate to solve both the non-linearities impairments and energy efficiency issues while keeping a high data rate thanks to bandwidth availability in the sub-THz bands.

APPENDIX
DATA FOR NON-LINEAR AM-AM & AM-PM MODELING

In this appendix, the numerical values of the parameters used to simulate photodiode non-linearities using the model derived in equations (4) and (5) are given in Tables 7 and 8 respectively.

TABLE 7. Parameters values for photodiode non-linearities AM-AM model.

Curve	g	a	b	c
α	0.65	5.7	-98.3	429.5
β	0.65	7	-219.4	1829

TABLE 8. Parameters values for PD non-linearities AM-PM model.

Curve	a	b	c	d	e	f
γ	-1.074	0.484	-0.037	7.861	-6.421	1.317
δ	-0.346	0.152	-0.013	2.392	-1.779	0.335

REFERENCES

[1] G. Ducournau, P. Szriftgiser, F. Pavanello, E. Peytavit, M. Zaknoune, D. Bacquet, A. Beck, T. Akalin, J.-F. Lampin, and J.-F. Lampin, "THz communications using photonics and electronic devices: The race to data-rate," *J. Infr., Millim., Terahertz Waves*, vol. 36, no. 2, pp. 198–220, Feb. 2015.

[2] T. Nagatsuma, "Advances in THz wireless communications," in *Proc. Conference Lasers Electro-Optics*, 2017, p. SM3J.

[3] T. Nagatsuma, "Advances in terahertz communications accelerated by photonics technologies," in *Proc. 24th OptoElectronics Commun. Conf. (OECC) Int. Conf. Photon. Switching Comput. (PSC)*, Jul. 2019, pp. 1–3.

[4] T. S. Rappaport, Y. Xing, O. Kanhere, S. Ju, A. Madanayake, S. Mandal, A. Alkhateeb, and G. C. Trichopoulos, "Wireless communications and applications above 100 GHz: Opportunities and challenges for 6G and beyond," *IEEE Access*, vol. 7, pp. 78729–78757, 2019.

[5] C. Chaccour, M. N. Soorki, W. Saad, M. Bennis, P. Popovski, and M. Debbah, "Seven defining features of terahertz (THz) wireless systems: A fellowship of communication and sensing," *IEEE Commun. Surveys Tuts.*, vol. 24, no. 2, pp. 967–993, 2nd Quart., 2022.

[6] C. Castro, R. Elschner, T. Merkle, C. Schubert, and R. Freund, "Long-range high-speed THz-wireless transmission in the 300 GHz band," in *Proc. 3rd Int. Workshop Mobile Terahertz Syst. (IWMTS)*, Jul. 2020, pp. 1–4.

[7] P. Rodríguez-Vázquez, M. E. Leinonen, J. Grzyb, N. Tervo, A. Parssinen, and U. R. Pfeiffer, "Signal-processing challenges in leveraging 100 Gb/s wireless THz," in *Proc. 2nd 6G Wireless Summit (6G SUMMIT)*, Mar. 2020, pp. 1–5.

[8] Z. Lai, C. Li, Y. Li, X. Lai, J. Li, and K. Guan, "A high-order modulation (64-QAM) broadband THz communication system over 100 Gbps," in *Proc. IEEE 4th Int. Conf. Electron. Inf. Commun. Technol. (ICEICT)*, Aug. 2021, pp. 553–556.

[9] E. Andrianopoulos et al., "Real-time sub-THz link enabled purely by optoelectronics: 90–310 GHz seamless operation," *IEEE Photon. Technol. Lett.*, vol. 35, no. 5, pp. 237–240, Mar. 1, 2023.

[10] J. Shi, Z. Li, J. Jia, Z. Li, C. Shen, J. Zhang, and N. Chi, "Waveform-to-Waveform end-to-end learning framework in a seamless fiber-terahertz integrated communication system," *J. Lightw. Technol.*, vol. 41, no. 8, pp. 2381–2392, Apr. 1, 2023.

[11] P. Sen, D. A. Pados, S. N. Batalama, E. Einarsson, J. P. Bird, and J. M. Jornet, "The TeraNova platform: An integrated testbed for ultra-broadband wireless communications at true terahertz frequencies," *Comput. Netw.*, vol. 179, Oct. 2020, Art. no. 107370.

[12] I. Kallfass, J. Antes, T. Schneider, F. Kurz, D. Lopez-Diaz, S. Diebold, H. Massler, A. Leuther, and A. Tessmann, "All active MMIC-based wireless communication at 220 GHz," *IEEE Trans. Terahertz Sci. Technol.*, vol. 1, no. 2, pp. 477–487, Nov. 2011.

[13] T. Nagatsuma, M. Sonoda, T. Higashimoto, L. Yi, and J. Hesler, "12.5-Gbit/s wireless link at 720 GHz based on photonics," in *Proc. 44th Int. Conf. Infr., Millim., Terahertz Waves (IRMMW-THz)*. Paris, France: IEEE, Sep. 2019, pp. 1–2.

[14] X. Yu, T. Miyamoto, K. Obata, Y. Hosoda, J.-Y. Kim, M. Fujita, and T. Nagatsuma, "Direct terahertz communications with wireless and fiber links," in *Proc. 44th Int. Conf. Infr., Millim., Terahertz Waves (IRMMW-THz)*. Paris, France: IEEE, Sep. 2019, pp. 1–2.

[15] Y. Horst, T. Blatter, L. Kulmer, B. I. Bitachon, B. Baeuerle, M. Destraz, W. Heni, S. Koepfli, P. Habegger, M. Eppenberger, E. D. Leo, C. Hoessbacher, D. L. Elder, S. R. Hammond, L. E. Johnson, L. R. Dalton, Y. Fedoryshyn, Y. Salamin, M. Burla, and J. Leuthold, "Transparent optical-THz-optical link at 240/192 Gbit/s over 5/115 M enabled by plasmonics," *J. Lightw. Technol.*, vol. 40, no. 6, pp. 1690–1697, Mar. 7, 2022.

[16] L. Moeller, J. Federici, and K. Su, "2.5 Gbit/s duobinary signalling with narrow bandwidth 0.625 terahertz source," *Electron. Lett.*, vol. 47, no. 15, p. 856, 2011.

[17] S. Jia, L. Zhang, S. Wang, W. Li, M. Qiao, Z. Lu, N. M. Idrees, X. Pang, H. Hu, X. Zhang, L. K. Oxenløwe, and X. Yu, "2 × 300 Gbit/s line rate PS-64QAM-OFDM THz photonic-wireless transmission," *J. Lightw. Technol.*, vol. 38, no. 17, pp. 4715–4721, Sep. 2020.

[18] D. Bodet, P. Sen, Z. Hossain, N. Thawdar, and J. M. Jornet, "Hierarchical bandwidth modulations for ultra-broadband communications in the terahertz band," *IEEE Trans. Wireless Commun.*, vol. 22, no. 3, pp. 1931–1947, Mar. 2023.

[19] P. Desombre, H. Farès, and Y. Louet, "Performance comparison of digital modulations in the presence of Gaussian phase noise in the sub-THz context," in *Proc. 4th Int. Workshop Mobile Terahertz Syst. (IWMTS)*. Essen, Germany: IEEE, Jul. 2021, pp. 1–5.

[20] T. F. Detwiler, S. M. Searcy, S. E. Ralph, and B. Basch, "Continuous phase modulation for fiber-optic links," *J. Lightw. Technol.*, vol. 29, no. 24, pp. 3659–3671, Dec. 7, 2011.

[21] P. Desombre, J. Taillieu, C. Tzimoragka, L. Bramerie, M. Gay, D. González Ovejero, M. Alouini, H. Farès, and Y. Louet, "Continuous phase modulations for sub-THz wireless communications," in *Proc. 35th Gen. Assem. Sci. Symp. Int. Union Radio Sci. (URSI GASS)*, Aug. 2023, pp. 1–3.

[22] (1994). *European Digital Cellular Telecommunications System (Phase 2); Modulation*. [Online]. Available: https://www.etsi.org/deliver/etsi_i_ets/300500_300599/300576/01_60/ets_300576e01p.pdf

[23] J. B. Anderson, T. Aulin, and C.-E. Sundberg, *Digital Phase Modulation*. Springer, 1986.

[24] G. Zhou and P. Runge, "Nonlinearities of high-speed p-i-n photodiodes and MUTC photodiodes," *IEEE Trans. Microw. Theory Techn.*, vol. 65, no. 6, pp. 2063–2072, Jun. 2017.

[25] C. C. Renaud, M. Natrella, C. Graham, J. Seddon, F. Van Dijk, and A. J. Seeds, "Antenna integrated THz uni-traveling carrier photodiodes," *IEEE J. Sel. Topics Quantum Electron.*, vol. 24, no. 2, pp. 1–11, Mar. 2018.

[26] P. Runge, F. Ganzer, T. Beckerwerth, S. Keyvaninia, S. Mutschall, A. Seeger, W. Ebert, and M. Schell, "Linearity of waveguide integrated modified uni-travelling carrier photodiode arrays," *IEEE Photon. Technol. Lett.*, vol. 31, no. 3, pp. 246–249, Feb. 8, 2019.

[27] J. P. Seddon, M. Natrella, X. Lin, C. Graham, C. C. Renaud, and A. J. Seeds, "Photodiodes for terahertz applications," *IEEE J. Sel. Topics Quantum Electron.*, vol. 28, no. 2, pp. 1–12, Mar. 2022.

[28] S. Khanra and A. Das Barman, "Linearity analysis of uni-traveling carrier photodiode for MM w applications," in *Proc. Int. Conf. Microw. Photon. (ICMAP)*, Dec. 2013, pp. 1–4.

[29] A. Beling, H. Pan, H. Chen, and J. C. Campbell, "Linearity of modified uni-traveling carrier photodiodes," *J. Lightw. Technol.*, vol. 26, no. 15, pp. 2373–2378, Jul. 5, 2008.

[30] H. Ito, A. Hirata, T. Minotani, Y. Hirota, T. Ishibashi, A. Sasaki, and T. Nagatsuma, "High-power photonic millimetre wave generation at 100 GHz using matching-circuit-integrated uni-travelling-carrier photodiodes," *IEE Proc. Optoelectronics*, vol. 150, no. 2, pp. 138–142, Apr. 2003.

[31] X. Lin, M. Natrella, J. Seddon, C. Graham, C. C. Renaud, M. Tang, J. Wu, H. Liu, and A. J. Seeds, "High performance waveguide uni-travelling carrier photodiode grown by solid source molecular beam epitaxy," *Opt. Exp.*, vol. 27, no. 25, p. 37065, Dec. 2019.

[32] L. Kang and B. H. Kolner, "Characterization of AM-to-PM conversion in silicon p-i-n photodiodes," *IEEE Photon. Technol. Lett.*, vol. 31, no. 13, pp. 1001–1004, Jul. 9, 2019.

[33] X. Xie, J. Zang, A. Beling, and J. Campbell, "Characterization of amplitude noise to phase noise conversion in charge-compensated modified unitravelling carrier photodiodes," *J. Lightw. Technol.*, vol. 35, no. 9, pp. 1718–1724, May 6, 2017.

[34] Y. Hu, C. R. Menyuk, X. Xie, M. N. Hutchinson, V. J. Urick, J. C. Campbell, and K. J. Williams, "Computational study of amplitude-to-phase conversion in a modified unitraveling carrier photodetector," *IEEE Photon. J.*, vol. 9, no. 2, pp. 1–11, Apr. 2017.

[35] Z. Song, Z. Zhou, J. Huang, X. Zou, C. Yang, and B. Chen, "Analysis of AM-to-PM conversion in MUTC photodiodes based on an equivalent circuit model," *Opt. Exp.*, vol. 29, no. 21, p. 33582, Oct. 2021.

[36] A. A. M. Saleh, "Frequency-independent and frequency-dependent nonlinear models of TWT amplifiers," *IEEE Trans. Commun.*, vols. COM-29, no. 11, pp. 1715–1720, Nov. 1981.

[37] K. Levenberg, "A method for the solution of certain non-linear problems in least squares," *Quart. Appl. Math.*, vol. 2, no. 2, pp. 164–168, 1944.

[38] D. W. Marquardt, "An algorithm for least-squares estimation of nonlinear parameters," *J. Soc. Ind. Appl. Math.*, vol. 11, no. 2, pp. 431–441, Jun. 1963.

[39] V. J. Urick, J. D. Mckinney, and K. J. Williams, *Fundamentals Microwave Photonics*. Hoboken, NJ, USA: Wiley, 2015.

[40] J. M. Senior and M. Y. Jamro, *Optical Fiber Communications: Principles and Practice*, 3rd ed., Upper Saddle River, NJ, USA: Prentice-Hall, 2009.

[41] N. A. Abbasi, A. Hariharan, A. M. Nair, and A. F. Molisch, "Channel measurements and path loss modeling for indoor THz communication," in *Proc. 14th Eur. Conf. Antennas Propag. (EuCAP)*, Mar. 2020, pp. 1–5.

[42] Y. Koda, N. Ohmi, H. Endo, and H. Harada. (2023). *105 GHz Multipath Propagation Measurements and Path Loss Model for Sub-THz Indoor Short-Range Communications*. [Online]. Available: https://www.techrxiv.org/articles/preprint/105_GHz_Multipath_Propagation_Measurements_and_Path_Loss_Model_for_Sub-THz_Indoor_Short-Range_Communications/23661519/1

[43] S. Ju and T. S. Rappaport, "142 GHz multipath propagation measurements and path loss channel modeling in factory buildings," in *Proc. IEEE Int. Conf. Commun.*, Jun. 2023, pp. 5048–5053.

[44] A. Andrae and T. Edler, "On global electricity usage of communication technology: Trends to 2030," *Challenges*, vol. 6, no. 1, pp. 117–157, Apr. 2015.

[45] W. Zhang, C.-X. Wang, D. Chen, and H. Xiong, "Energy-spectral efficiency tradeoff in cognitive radio networks," *IEEE Trans. Veh. Technol.*, vol. 65, no. 4, pp. 2208–2218, Apr. 2016.

[46] E. Li, W. Zhang, J. Sun, C.-X. Wang, and X. Ge, "Energy-spectral efficiency tradeoff of visible light communication systems," in *Proc. IEEE/CIC Int. Conf. Commun. China (ICCC)*, Jul. 2016, pp. 1–5.

[47] L. Deng, Y. Rui, P. Cheng, J. Zhang, Q. T. Zhang, and M. Li, "A unified energy efficiency and spectral efficiency tradeoff metric in wireless networks," *IEEE Commun. Lett.*, vol. 17, no. 1, pp. 55–58, Jan. 2013. http://ieeexplore.ieee.org/document/6365872/

[48] B. De Beelde, D. Plets, E. Tanghe, and W. Joseph, "Directional sub-THz antenna-channel modelling for indoor scenarios," in *Proc. 15th Eur. Conf. Antennas Propag. (EuCAP)*, Mar. 2021, pp. 1–4.

[49] Y. Xing and T. S. Rappaport, "Propagation measurements and path loss models for sub-THz in urban microcells," in *Proc. ICC IEEE Int. Conf. Commun.*, Jun. 2021, pp. 1–6.

[50] *RECOMMENDATION ITU-R P.676-13—Attenuation By Atmospheric Gases and Related Effects*, Standard ITU-R P.676-1, ITU, 2022, p. 676.

[51] D. Stanze, A. Deninger, A. Roggenbuck, S. Schindler, M. Schlak, and B. Sartorius, "Compact cw terahertz spectrometer pumped at 1.5 μm wavelength," *J. Infr., Millim., Terahertz Waves*, vol. 32, no. 2, pp. 225–232, Feb. 2011.

[52] K. Kassan, H. Farès, D. C. Glattli, and Y. Louet, "Performance vs. Spectral properties for single-sideband continuous phase modulation," *IEEE Trans. Commun.*, vol. 69, no. 7, pp. 4402–4416, Jul. 2021.

[53] K. Kassan, H. Farès, D. C. Glattli, and Y. Louet, "Simplified receivers for generic binary single side band CPM using PAM decomposition," *IEEE Access*, vol. 9, pp. 115962–115971, 2021. https://ieeexplore.ieee.org/document/9516015/

[54] J. G. Proakis and D. G. Manolakis, *Digital Signal Processing: Principles, Algorithms, and Applications*, 3rd ed. Upper Saddle River, NJ, USA: Prentice-Hall, 1996.

[55] J. Kokkoniemi, A.-A.-A. Boulogeorgos, M. Aminu, J. Lehtomäki, A. Alexiou, and M. Juntti, "Impact of beam misalignment on THz wireless systems," *Nano Commun. Netw.*, vol. 24, May 2020, Art. no. 100302.

[56] J. G. Proakis and M. Salehi, *Digital Communications*. New York, NY, USA: McGraw-Hill, 2008.

[57] V. Petrov, A. Pyattaev, D. Moltchanov, and Y. Koucheryavy, "Terahertz band communications: Applications, research challenges, and standardization activities," in *Proc. 8th Int. Congr. Ultra Modern Telecommun. Control Syst. Workshops (ICUMT)*. Lisbon, Portugal: IEEE, Oct. 2016, pp. 183–190.

[58] I. F. Akyildiz, J. M. Jornet, and C. Han, "Terahertz band: Next frontier for wireless communications," *Phys. Commun.*, vol. 12, pp. 16–32, Sep. 2014.

[59] Y. Katayama, K. Takano, Y. Kohda, N. Ohba, and D. Nakano, "Wireless data center networking with steered-beam mmWave links," in *Proc. IEEE Wireless Commun. Netw. Conf.*, Mar. 2011, pp. 2179–2184.

[60] K. Wu, J. Xiao, and L. M. Ni, "Rethinking the architecture design of data center networks," *Frontiers Comput. Sci.*, vol. 1, no. 2, pp. 1–24, Sep. 2012.

[61] T. S. Rappaport, Y. Xing, G. R. MacCartney, A. F. Molisch, E. Mellios, and J. Zhang, "Overview of millimeter wave communications for fifth-generation (5G) wireless networks—With a focus on propagation models," *IEEE Trans. Antennas Propag.*, vol. 65, no. 12, pp. 6213–6230, Dec. 2017.

[62] M. Z. Chowdhury, Md. Shahjalal, S. Ahmed, and Y. M. Jang, "6G wireless communication systems: Applications, requirements, technologies, challenges, and research directions," *IEEE Open J. Commun. Soc.*, vol. 1, pp. 957–975, 2020.

[63] S. Dang, O. Amin, B. Shihada, and M.-S. Alouini, "What should 6G be?" 2019, *arXiv:1906.00741*.

[64] Z. Chen, C. Han, Y. Wu, L. Li, C. Huang, Z. Zhang, G. Wang, and W. Tong, "Terahertz wireless communications for 2030 and beyond: A cutting-edge frontier," *IEEE Commun. Mag.*, vol. 59, no. 11, pp. 66–72, Nov. 2021.

[65] P. Laurent, "Exact and approximate construction of digital phase modulations by superposition of amplitude modulated pulses (AMP)," *IEEE Trans. Commun.*, vols. COM-34, no. 2, pp. 150–160, Feb. 1986.

[66] U. Mengali and M. Morelli, "Decomposition of Mary CPM signals into PAM waveforms," *IEEE Trans. Inf. Theory*, vol. 41, no. 5, pp. 1265–1275, Sep. 1995.

[67] E. Perrins and M. Rice, "A new performance bound for PAM-based CPM detectors," *IEEE Trans. Commun.*, vol. 53, no. 10, pp. 1688–1696, Oct. 2005.

[68] E. S. Perrins, "Reduced complexity detection methods for continuous phase modulation," M.S. thesis, Dept. Elect. Comput. Eng., Brigham Young Univ., Provo, UT, USA, Dec. 2005.

[69] M. Saad, F. Bader, J. Palicot, A. C. A. Ghouwayel, and H. Hijazi, "Single carrier with index modulation for low power terabit systems," in *Proc. IEEE Wireless Commun. Netw. Conf. (WCNC)*. Marrakesh, Morocco: IEEE, Apr. 2019, pp. 1–7.

[70] M. Saad, F. C. Lteif, A. C. Al Ghouwayel, H. Hijazi, J. Palicot, and F. Bader, "Generalized spatial modulation in highly correlated channels," in *Proc. IEEE 30th Int. Symp. Pers., Indoor Mobile Radio Commun.*, Sep. 2019, pp. 1–6.

[71] A. Younis, N. Serafimovski, R. Mesleh, and H. Haas, "Generalised spatial modulation," in *Proc. Conf. Rec. Forty 4th Asilomar Conf. Signals, Syst. Comput.*, Nov. 2010, pp. 1498–1502.

[72] J. Wang, S. Jia, and J. Song, "Generalised spatial modulation system with multiple active transmit antennas and low complexity detection scheme," *IEEE Trans. Wireless Commun.*, vol. 11, no. 4, pp. 1605–1615, Apr. 2012.

[73] T. Datta and A. Chockalingam, "On generalized spatial modulation," in *Proc. IEEE Wireless Commun. Netw. Conf. (WCNC)*, Apr. 2013, pp. 2716–2721.

[74] W. Saad, M. Bennis, and M. Chen, "A vision of 6G wireless systems: Applications, trends, technologies, and open research problems," *IEEE Netw.*, vol. 34, no. 3, pp. 134–142, May 2020.

PAUL DESOMBRE (Member, IEEE) received the Engineer and M.Sc. degrees in telecommunications from INP-ENSEEIHT of Toulouse, in 2020. He is currently pursuing the Ph.D. degree in telecommunications with CentraleSupélec-Rennes Campus, France. He has a temporary teacher position with the Electronics and IT Department, Rennes University, France. His research interests include sub-THz wireless communications, optical communications, non-linearity impairments, and green communications.

HAÏFA FARÈS (Member, IEEE) received the bachelor's and M.Sc. degrees in telecommunication engineering from the Higher School of Communications of Tunis (SupCom), in 2007 and 2008, respectively, and the Ph.D. degree in digital communications from IMT-Atlantique, France, in 2011. She is currently an Associate Professor with CentraleSupélec-Rennes Campus. She is a member with the SIGNAL Research Group, CNRS Institute of Electronics and Digital Technologies (IETR), Rennes Laboratory. Her research interests include the area of communication theory, including nonlinear modulations, green communications, iterative decoding algorithms, and non-orthogonal multiple access.

YVES LOUËT received the Ph.D. degree in digital communications and the Habilitation degree from Rennes University, France, in 2000 and 2010, respectively. He joined CentraleSupélec-Rennes Campus, in 2002. He is currently a Full Professor with CentraleSupélec-Rennes Campus. He is the Head of the Signal and Communication Department, IETR Laboratory, CNRS. He was the Head of URSI Commission C, from 2015 to 2023. His topics regard signal processing and digital communications applied to software and cognitive radio systems, especially related to new waveforms design for green cognitive radio, and energy efficiency enhancement.